Materials & Design 227 (2023) 111696

Contents lists available at ScienceDirect

Materials & Design

journal homepage: www.elsevier.com/locate/matdes

Enhancing the prediction quality of mechanical properties for powder bed fusion with laser beam by dynamic observation of flying particles

Keisuke Nagato [a,*], Tomohiro Ozawa [a], Manuela Neuenfeldt [b], Frederik Zanger [b], Moju Zhao [a], Volker Schulze [b]

[a] Department of Mechanical Engineering, Graduated School of Engineering, The University of Tokyo, 7-3-1 Hongo, Bunkyo-ku, Tokyo 113-8656, Japan
[b] wbk Institute of Production Science, Karlsruhe Institute of Technology (KIT), Kaiserstrasse 12, 76131 Karlsruhe, Germany

HIGHLIGHTS

- The proposed system demonstrated the enhancement of prediction quality of mechanical properties in powder bed fusion with a laser beam.
- Flying particles, powder and droplet spatter, were dynamically observed using pulsed laser illumination and high-speed microscopy.
- The prediction score of Vickers hardness of the bulk sample was improved when using the spatter number.
- This method will lead to a higher-throughput exploration of process parameters also for other than aluminum alloy that was demonstrated.

GRAPHICAL ABSTRACT

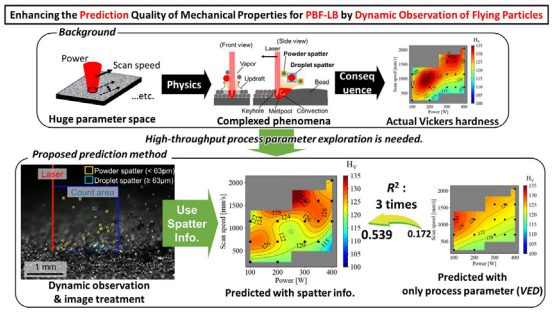

ARTICLE INFO

Article history:
Received 31 October 2022
Revised 18 January 2023
Accepted 3 February 2023
Available online 7 February 2023

Keywords:
Powder bed fusion
Dynamic observation
Spatter
Pulsed-laser illumination
Regression

ABSTRACT

Complex phenomena occur at the laser spot in powder bed fusion with laser beam (PBF-LB); thus, it creates several large process-parameter spaces such as power and scanning speed, along with many others. To allow for high-throughput parameter exploration, an efficient prediction method is necessary. To enhance the prediction quality of the mechanical properties, this paper proposes that the information collected from flying spatter particles, which are dominant in selective laser melting phenomena, can be used as feature values. Flying particles were dynamically observed using pulsed laser illumination and high-speed microscopy. Image treatment was used to detect both powder and droplet spatter, and it was possible to differentiate these two by assessing particle size—63 μm—which enables the quantification of each type. This approach was used at various laser powers and scanning speeds to characterize the single-bead shapes, porosity, and Vickers hardness for each parameter. The correlation between the counted amount of spatter and mechanical properties was investigated using regression analysis. The prediction accuracy of Vickers hardness using the volumetric energy density was observed to improve, with the coefficient of determination increasing from 0.172 to 0.539 when adding the amounts of powder and droplet spatter.

* Corresponding author.
E-mail address: nagato@hnl.t.u-tokyo.ac.jp (K. Nagato).

https://doi.org/10.1016/j.matdes.2023.111696
0264-1275/

1. Introduction

Among metallic additive manufacturing methods [1], powder bed fusion with a laser beam (PBF-LB) has the advantage of relatively high-dimensional accuracy because laser scanning on the powder bed improves local heating, melting, cooling, and solidification [2,3]. Compared with conventional forming processes such as forging and casting, and subtractive manufacturing processes such as cutting and grinding, complex shapes can be formed because there are no restrictions such as the size of the mold or tool paths. In addition, because it is a melt process, it is possible to process difficult to cut materials having high melting points [4,5]. Owing to the increase in industrial applications of reasonably priced high-output lasers, the throughput and quality have improved in recent years. These lasers are utilized in applications ranging from prototyping to small-lot and high-mix production. The physical phenomena of laser absorption, heat conduction, melting, evaporation, and solidification occur microscopically at high speeds at the point of laser irradiation. Because the phenomena are complex, further clarification of the modeling mechanism is necessary to determine the process parameters for desirable mechanical properties and shape accuracy. At the laser irradiation point, each powder behaves differently at low and high speeds with respect to phenomena such as laser absorption, heat generation, melting, decrease in contact heat resistance between particles, heat conduction, evaporation, surface waviness owing to the recoil pressure from evaporation, and decrease in viscosity [6,7]. In general, the recoil pressure creates a keyhole and produces a melt pool with a high aspect ratio. By accurately controlling these properties, precise manufacturing in the planar direction can be realized [8]. For optimal keyhole and melt pool shapes, the evaporation of material should be controlled; however, because evaporation is a divergent phenomenon, the mechanism of vapor [9,10] or spatter [11–13] should be clarified. Spatter is one of the feature values indicative of a physical phenomenon. Previous research has studied the relationship between spatter and sample properties such as single bead continuity [14], degree of oxidation [15], morphology of single beads [16], melt pool behavior [17], plume signature [18], and surface roughness [19]; however, these characteristics are indirect indicators of the mechanism at the point of laser irradiation.

The relationships between the spatter and the final mechanical properties were studied by investigating the porosity [20,21], microstructures [22–24], tensile strength [25], and roughness [26] of a variety of materials. Meanwhile, to model the high-speed microscopic physical phenomena at the point of laser irradiation, simulations were used to clarify the thermo-fluid dynamics [27–33]. Simultaneously, real-time observation techniques have been used to clarify these high-speed microscopic mechanisms [33]. Previous research has demonstrated high-resolution observations inside the melt pool through X-rays [34], observation of the melt-pool surface using a high-speed camera [35–37], and acquisition of temperature information [38]. These high-speed microscopic observations support the evaluation of the heat flow phenomenon and the creation of spatter [39,40]. Although it is certain that flying particles dominate the mechanical properties, no research has been conducted to predict their exact relationship. Moreover, there has been no systematic investigation of the correlation between the spatter phenomenon and the beads and bulk samples.

In this study, we propose the use of flying spatter particles to enhance the prediction quality of mechanical properties. We built an in situ observation system to directly observe the flight of particles, droplet spatter, and powder spatter in detail using pulsed-laser irradiation. Pulsed-laser irradiation suppresses the information of laser scattering, plasma radiation, and heat radiation of the processing laser using the laser power and scanning speed as parameters. The amount of spatter must reflect the physical phenomena of the PBF, and because it is related to the quality of the formed samples more than the process parameters, the amount of spatter was analyzed using a regression method. The porosity and mechanical properties were predicted by counting the amount of spatter droplets. Simultaneously, a conventional ex situ investigation was carried out for various aspects, such as single-bead shape, porosity, Vickers hardness, and grain size. This research is not expected to directly clarify the physical mechanism but to open a window to obtain the intermediate parameters required to predict the final performance values, such as mechanical properties, in real time. This technique can lead to high-throughput optimization in a large process-parameter exploration space.

2. Experimental setup of powder bed fusion

2.1. PBF-LB process parameters and material

The machine used was an SLM280HL from SLM Solutions Co. ltd. The powdered material used was a general aluminum alloy, LSM-I AlSi10Mg, m4p^{TM} material solutions GmbH (average diameter: 35 μm, lower diameter: 15 μm, upper diameter: 63 μm), which is generally used in PBF-LB. The PBF process parameters were varied as shown in Table 1. Parameters other than power and scanning speed were recommended by SLM Solutions Co., ltd. as a "standard recipe". The laser power and scanning speed for the observations were varied with the other parameters suggested by the standard recipe. Because the heat condition for observation was fixed in this study, the bulk layers were printed with the standard recipe each time before printing single beads.

Energy is usually indicated by the volumetric energy density (*VED*) [J/mm^3], which indicates the energy density per unit volume of powder, as shown in Eq. (1)

$$VED = \frac{P}{V d_{\mathrm{hatch}} t_{\mathrm{layer}}} \tag{1}$$

where P is the power [W], V is the scanning speed [mm/s], d_{hatch} is the hatch distance [mm], and t_{layer} is the thickness of the powder bed [mm].

Fig. 1 shows the *VED* in the parameter space used in this study.

2.2. Ex situ investigation

The samples were characterized ex situ by various measurements: width and shape of single beads, porosity, and Vickers

Table 1
PBF Parameters and Powder Information.

	Value
Laser wavelength	1070 [nm] (Fiber laser)
Laser spot	83 [μm]
Laser power (P)	100–400 [W] (Standard recipe; 350)
Laser scanning speed (V)	250–2050 [mm/s] (Standard recipe; 1150)
Hatch distance (d_{hatch})	170 [μm]
Layer thickness (t_{layer})	50 [μm]
Rotation angle hatch direction for each layer in bulk samples	77
Platform temperature	200 [°C]
Powder material	AlSi10Mg
Powder size (measured by m4p material solutions GmbH)	Average diameter: 35 μm Lower diameter: 15 μm Upper diameter: 63 μm

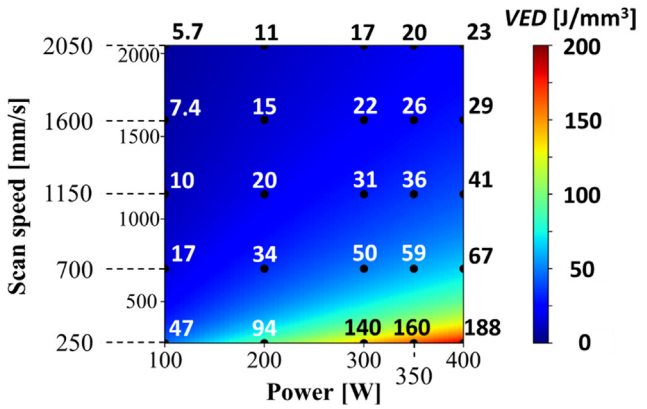

Fig. 1. Volumetric energy density distribution in parameter space for this study.

hardness of bulk samples. The cross-sections of the single beads were observed using optical microscopy (OLS-4500, OLYMUPS ltd.) to investigate the excess or deficiency of energy. The cross-sectional surfaces were polished, and the crystallinity was revealed by a mild fluorine-nitric acid treatment to show the boundary between the prior melt pool and the preliminarily formed base bed. The porosity was validated with three-dimensional X-ray computer tomography (3D-XCT, ZEISS METROTOM 800, Carl Zeiss) using bulk samples with dimensions of 10 × 10 × 10 mm^3. The imaging resolution was 5 μm. The tensile stress was validated using a Vickers hardness machine (HMV-G 21ST, Shimadzu, Co. ltd.). The grain size was characterized via scanning electron microscopy-electron back-scattering diffraction (SEM-EBSD, JSM-7100, JEOL ltd.).

3. Method of dynamic observation and image analysis

3.1. Principle of pulse-laser illumination

In the case of observation with normal optics, it is difficult to capture the structural information at the point of laser irradiation because the light from the PBF laser is scattered by the surface, plume (i.e., plasma light), and radiated light owing to the high-temperature surfaces that shine into the camera, as shown in Fig. 2(a). Even with a filter, which removes the PBF laser wavelength, the wavelength of the plume is broad and the white illumination may disrupt the surface information of the melt pool or spatter shape. A pulsed laser illumination system was used in this study, as shown in Fig. 2(b). When the laser energy in one pulse is higher than the power of the plasma at the same wavelength through the band-pass filter, the illuminating light scattered by the solid surfaces can be captured. This allows the collection of information on the bead surface and flying particles. Furthermore, the actual capture time corresponding to an efficient shutter speed is defined by the laser pulse width, and observations can be made at higher speeds than the camera shutter speed.

3.2. Experimental setup for in-situ observation

A laser irradiation system and camera were installed inside the PBF-LB apparatus. Fig. 3 shows a photograph of the experimental setup. From the left side of the glove-mounting flange, a high-speed camera (FastCam Mini AX100, Photron ltd.) with a micro lens (VSZ-0745 + VSZ-05X, vS Technology, ltd.) and band-pass filter (645+/-10 nm (full width at half maximum;)) were installed. To realize a working distance of 200 mm, even when the recoater moved forward, an additional window was placed inside the chamber. The part of the powder bed closest to the camera was used as the observation area. The height from the center of the lens to the powder bed surface was 95 mm, the capture angle was 25°, and the focus depth was 0.5 mm. The optical fiber for pulsed laser illumination (CAVILUX HF, Cavitar ltd.) was installed into the chamber through a feed through on the right side of the glove-mounting flange. The focusing lens for laser illumination was attached inside the chamber so that the pulse laser illuminated the observation area from the opposite side. The illumination from the opposite side enhances the spatial resolution more than that from the front.

3.3. Parameters for observation optics

Tables 2 and 3 show the illumination parameters of the CAVILUX HF (Cavitar ltd.) and the high-speed camera parameters of the FastCam Mini (Photron ltd.).

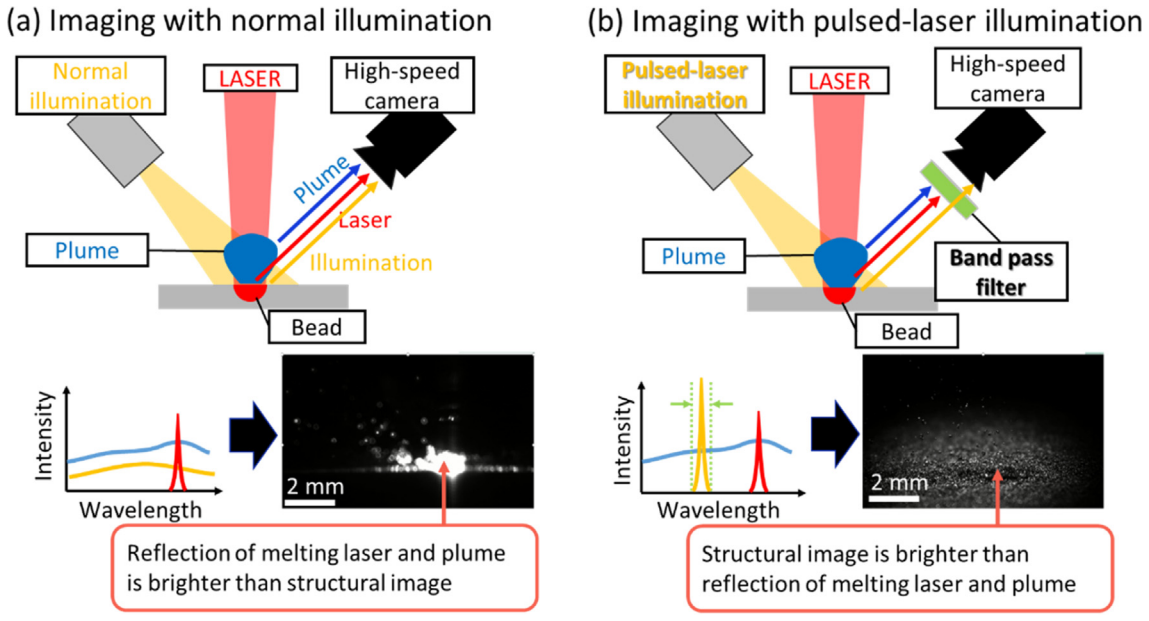

Fig. 2. Schematics of observation systems (a) without and (b) with pulsed-laser illumination.

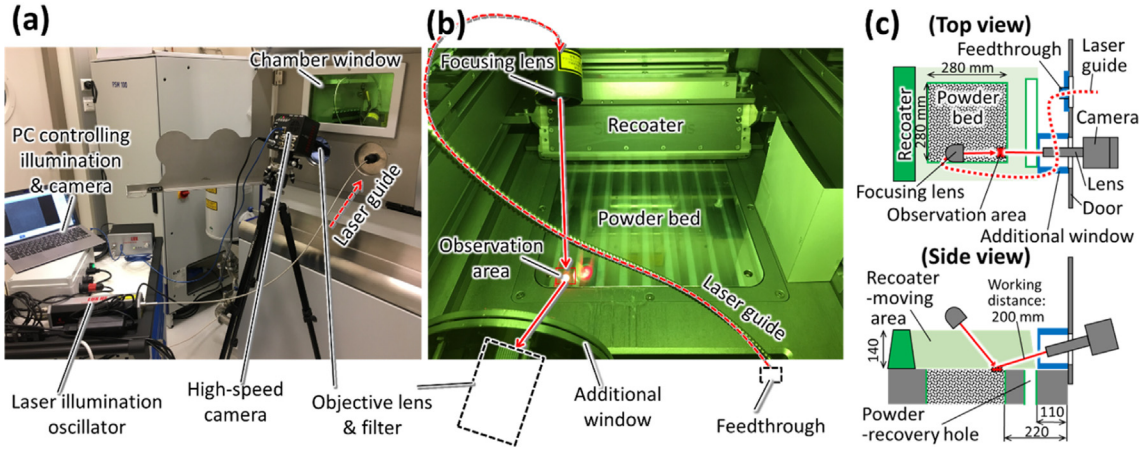

Fig. 3. Experimental setup; photographs of appearance (a), inside chamber(b), and dimension(c).

Table 2
Illumination parameters.

	Value
Illumination power	280 [W]
Wavelength	640 [nm]
Spot size	ϕ 10 [mm]
Frequency	6,000 fps (as camera frame rate)
Pulse width	40 [ns]
Delay time to camera shutter	1.2 [μs]

Table 3
Camera Parameters.

	Value
Captured area	10 mm in width
Frame rate	6,000 fps
Shutter speed	10 μs (1/100,000 s)
Pixel number	1024 × 736
Capture size for pixel	5 μm
Working distance of lens	200 mm
Band pass filter	645 +/- 10 (FWHM)

First, the definition of spatial resolution was described. The captured area and spot size were set to 10 mm in width so that there was sufficient space to capture the flying particles. The width resolution of the camera in this study was set to 1,024 pixels, and the spatial resolution was approximately 10 μm, which could capture original powder particles with a diameter of 35 μm and a larger spatter. Next, the definition of the time resolution was defined. The camera frame rate was set to 6,000 fps, which could capture a particle flying at 1 m/s at approximately 170 μm intervals. Because the laser power was limited, the pulse width and frequency exhibited a trade-off relationship. Thus, the pulse width was set to the maximum value of 40 ns. At this efficient shutter speed, a particle flying at 1 m/s moves approximately 40 nm, which is much smaller than that required for good spatial resolution. The delay time of the laser after the camera shutter opened was set to 1.2 μs, which was shorter than the shutter speed of the camera. The shutter speed of the camera was set at a short limit of 10 μs (100,000 fps). We confirmed that when the shutter speed was longer than 100 μs (10,000 fps), light from the plasma interfered with the camera.

3.4. Image treatment

This section describes the details of the image treatment process that differentiates small particles from the spatter and counts them. We applied the border following method (BFM) [41] in which a white continuous image is judged as an object in a binary image. A pre-treatment that causes the particles to stand out from the background is important because there are particles on the powder bed which are obscured by the flying out of focus particles, as shown in Fig. 4(a) but can affect the final count. During pre-treatment, the brightness and contrast were adjusted to minimize the signal received from the background compared to the flying particles. The stationary particles around the bead were in focus, as were the moving particles to be counted. In this study, they were separated using the frame difference method (FDM) [42,43]. Another method, called the background subtraction method, was not suitable because some particles would drop onto the powder bed and change the background. In the FDM, two different images were produced from three continuous frames and the logical AND conjunction. The results of the images were binarized, and the moving objects were detected by the BFM. We confirmed that only the flying particles separated the stationary particles, and no background image was used.

We could not distinguish the flying particles from the original powder or melted powder because the observation method only captured structural information. Therefore, in this study, we defined particles larger than 63 μm, which was the upper diameter of the original powder, as shown in Table 1, as droplet spatter. Although particles with a diameter of 63 μm or smaller may also have included droplet spatter, we defined all the smaller particles as powder droplets in this study. To definitively distinguish between them, we had to obtain other information, such as temperature or surface roughness, which may have differed between the as-received powder and droplet powder. The as-received powder would have a rougher surface because it was atomized, solidified, and exposed to the atmosphere once, whereas the droplet powder would have a smoother surface because it melted in argon gas and had a liquid surface or new face even after solidifying. Such an investigation should be conducted in the future.

We describe the definition of powder spatter and droplet powder again from the viewpoint of image treatment. We defined larger particles covering nine pixels or more, i.e., 63.4 μm or more, as droplet spatter, and smaller particles covering eight pixels or less, i.e., 56 μm or less, as powder spatter. The count area was defined as 200 × 200 pixels, i.e., 1.76 × 1.76 mm^2 behind the laser and above the bead as shown in Fig. 4(a). Fig. 4(b-1) and (b-2) show examples of captured particles as powder spatter and droplet spatter, respectively. Fig. 4(c) shows an example of the transition of the count number as a function of the frame number when the laser power, scanning speed, and *VED* were 350 W, 1600 mm/s, and 26 J/mm^3,

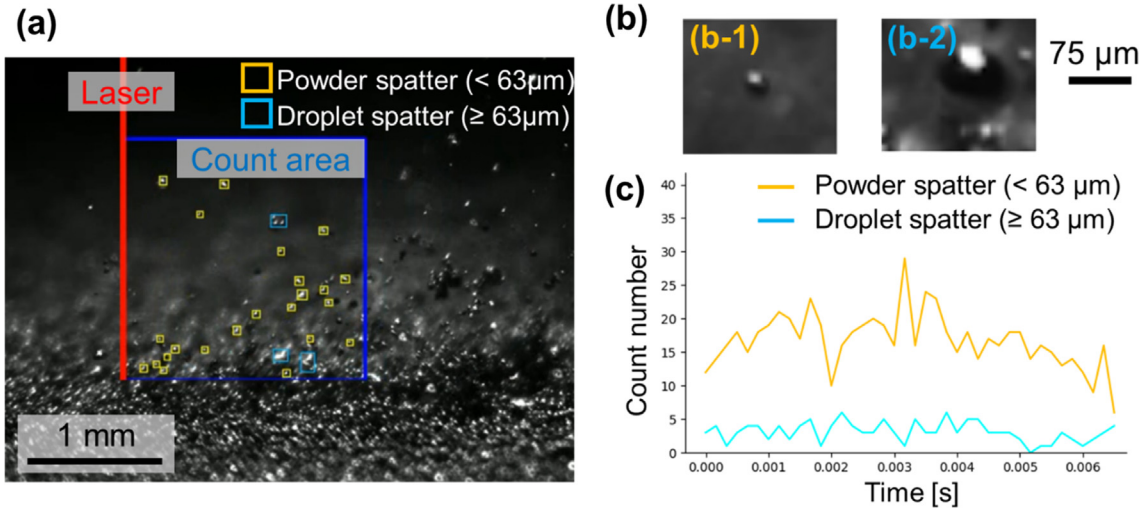

Fig. 4. An example of image treatment (power: 350 W, scanning speed: 1,600 mm/s); (a) particles smaller and greater than 63 μm were captured in the 1.76 × 1.76 mm^2 area behind laser and above the bead, (b) examples captured as (b-1) powder spatter and (b-2) droplet spatter, (c) temporal transition of count number of the small particles and spatter.

respectively. The average numbers of small particles and spatter were used to investigate the flying particle phenomenon in the following sections. As described in Section 3.2, the depth of focus was 0.5 mm. The particles in the foreground or background were out of depth and were not captured in the images because they were blurred, and the brightness of the focused illumination was low.

3.5. Regression analysis of mechanical properties by amount of spatter

The mechanical properties, such as porosity and Vickers hardness, must be strongly related to the *VED*; however, the spatter data represent the physical phenomena at the intermediate relationship between the process parameters (power and scanning speed in this study) and final performance values (porosity and Vickers hardness in this study). Therefore, we introduced an exponential model to predict the mechanical properties from a process parameter, the *VED*, as follows:

$$val_{po} = \mu_{po} VED^{\alpha_{po}} \tag{2}$$

$$val_{vh} = \mu_{vh} VED^{\alpha_{vh}}, \tag{3}$$

where val_{po} and val_{vh} are the values denoting the porosity and Vickers hardness, respectively, and the *VED* is described by Eq. (1). These equations integrate the influence of laser power and scanning speed into a single value. Here, α_{po} and α_{vh} are the exponents and μ_{po} and μ_{vh} are the multiplication rates.

To investigate the effect of spatter data mathematically predicting the mechanical properties, we further introduced the number of powder and droplet spatters as prediction variables. The extended nonlinear model from (2) and (3) can then be written as

$$val_{po} = \mu_{po} VED^{\alpha_{po}} n_p^{\beta_{po}} n_d^{\gamma_{po}} \tag{4}$$

$$val_{vh} = \mu_{vh} VED^{\alpha_{vh}} n_p^{\beta_{vh}} n_d^{\gamma_{vh}}, \tag{5}$$

where n_p and n_d denote the number of powder and droplet spatters, respectively, and β_{po}, β_{vh}, γ_{po}, and γ_{vh} are the corresponding exponents for each base.

To obtain the exponents and base values in Eqs. (4) and (5), a regression process was applied. Among the various regularized regression methods [44], ridge regression [45] has the fastest computation owing to the L2-norm penalty for regularization. However, we chose the least absolute shrinkage and selection operator (LASSO) [46] because it uses an L1-norm penalty for regularization, which can reduce the coefficient of the less important variable to almost zero. Thus, irrelevant variables can be disregarded. To obtain a linearized model for regression, a logarithmic transformation was performed for Eqs. (4) and (5). Then, the loss function of the LASSO regression can be expressed as

$$\sum_{i=1}^{n} \left(y_i - \sum_{j=1}^{4} k_j x_{ij} \right)^2 + \lambda \sum_{j=1}^{4} |k_j|, \tag{6}$$

where y_i corresponds to $\log(val_{po})$ for Eq. (4) or $\log(val_{vh})$ for Eq. (5), and i denotes the i-th regression data. x_{ij} is logarithmically transformed data, including $\log(VED)$, $\log(n_p)$, and $\log(n_{drop})$. We also introduced a constant variable, $x_{i4} = 1$ for the multiplication factor μ. k_j denotes the coefficients in the linearized model using logarithmic transformation ($k_1 = \alpha_{po}, k_2 = \beta_{po}, k_3 = \gamma_{po}$, and $k_4 = \log(\mu_{vh})$ for Eq. (4); $k_1 = \alpha_{vh}, k_2 = \beta_{vh}, k_3 = \gamma_{vh}$, and $k_4 = \log(\mu_{vh})$ for Eq. (5)). The second term in Eq. (6) represents regularization using the L1 norm, and λ is the regularization coefficient.

The regression process can also be applied to the basic exponential models in Eqs. (2) and (3). In this study, we compared the regression results between these basic models (Eqs. (2) and (3)) and the extended models (Eqs. (4) and (5)) to evaluate the positive influence of having more variables (i.e., n_p and n_d) on the prediction.

4. Results of ex-situ validation of bulk test pieces

4.1. Single bead

Fig. 5(a) shows cross-sectional optical images of single beads produced using 25 parameter sets. The base surfaces were prepared using the normal recipe for bulk samples, and the internal materials were sufficiently dense. "N/A," shown on the upper left parameter areas, means the single beads were not successfully fabricated because the *VED*s were too low. The red line in each microscope image shows the boundary of the prior-melt pool, which was differentiated by the contrast in crystallinity between the preliminarily formed base. Fig. 5(a) indicates four categories: (a-1)-(a-4). In (a-1) the prior melt pool depth was larger than the bead height because the *VED* was at a minimum where the keyhole and melt

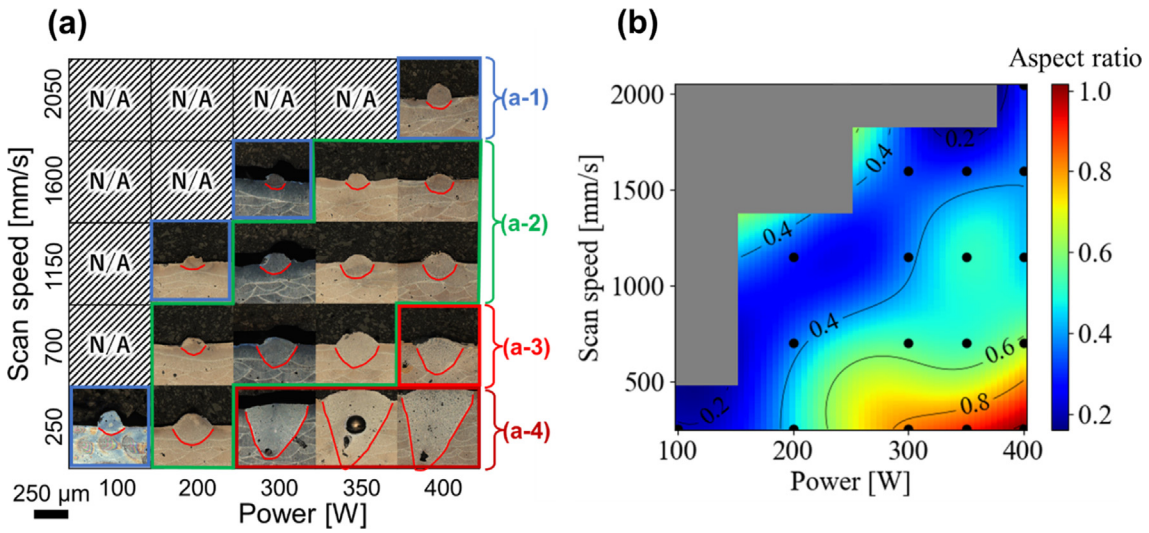

Fig. 5. (a) Cross-sectional optical microscope images of single beads, and (b) plots of aspect ratio as functions of power and scanning speed. (a-1)–(a-4): character categories.

pool reached the base surface and the bead could be formed. In (a-2), the prior melt pool depth was appropriate and beads were stably formed, which means that the *VED*s were comparatively appropriate at 26–94 J/mm^3. In (a-3) the bead height was low, had a few minor porosities, and the prior melt pool depth was comparatively deep, which means that the *VED* was too high. In (a-4) the melt pool depths were large, the beads were twice as wide as the laser spot diameter (300 μm), and pores due to bubbles were observed, which means that the *VED*s were clearly too high. As described in the following section, bulk samples were not successfully formed with the parameters of (a-4).

Fig. 5(b) presents the plot of the aspect ratio of the beads, which was calculated using the width and total height of the bead including the convex area higher than the base surface underneath and the melt pool area inside the bases. There was a valley from the bottom left to the upper right. This belt corresponds to category (a-2). The aspect ratio in categories (a-1) and (a-3) approached a median value, whereas category (a-4) showed an aspect ratio greater than 0.8.

4.2. Porosity of bulk sample by 3D-XCT

Fig. 6(a) and (b) show the cross-sectional optical and contour images of the volumetric porosity, respectively, obtained by 3D-XCT. Because of the low *VED* (upper left), bulk samples were not obtained as the melt pool was not deep enough. Samples with powers of 100 W at 700 mm/s and 1150 mm/s were obtained, even though the single beads were not. This is because the hatching process imparted a larger amount of energy per unit area on the powder bed, and each bead was connected to its neighbor. Therefore, the clearance between solid phase was 100–300 μm, which is the same as or greater than the spot diameter and hatch distances. Simultaneously, three samples with higher *VED*s were not successfully obtained. This is because the imparted energy was so great that the melt pool had an excessive width and depth, as shown in Fig. 5(a), and the surface of the bed was too wavy to recover successfully. Fig. 6(b) shows areas with decreasing porosity from the bottom left to the top right. As previously described, the areas on the left side had insufficient energy to completely melt the powders (lower *VED* than appropriate). In contrast, in the areas on the right side, pores are formed owing to the blow holes (higher *VED* than appropriate) [47].

4.3. Vickers hardness and microstructure

Fig. 7(a) shows the Vickers hardness as a function of the *VED*. The grain size of these samples was analyzed using SEM-EBSD analysis. The grains were defined as large-angle grain boundaries (greater than15°). Fig. 7(b) shows the Vickers hardness as a function of the mean grain size. Note that the grain sizes of the samples with *VED*s of 10 J/mm^3 (100 W, 1150 mm/s) and 16 J/mm^3 (100 W, 700 mm/s) could not be characterized because their porosities were too large at 41 % and 31 %, respectively. Fig. 7(c) shows the inverse pole figure (IPF) maps of the samples (c-1) 300 W, 1600 mm/s (*VED*: 22), (c-2) 350 W, 1150 mm/s (*VED*: 36), (c-3) 400 W, 700 mm/s (*VED*: 67), and (c-4) 200 W, 250 mm/s (*VED*: 94).

As shown in Fig. 7(a), the Vickers hardness increased to 133 HV at a *VED* of 20 J/mm^3, decreased to 107 HV at a *VED* of 70 J/mm^3, and finally increased again to 116 HV at a *VED* of 94 J/mm^3. The porosities of the samples with *VED*s of 10 and 17 J/mm^3 (white circles in Fig. 7(a)) were too large to precisely characterize the Vickers hardness. This is because when the indenter pushes against the surface, any voids present underneath will collapse, and the HV value will be lower than the actual hardness. The higher standard deviations in these two samples support this finding. To characterize the hardness more precisely, nano indentation was performed. Also in Fig. 7(a), the Vickers hardness decreases to 107 HV from 135 HV due to the difference in grain size, as shown in Fig. 7(b). The mean grain size was distributed from 7.4 μm to 11.7 μm for 107 HV–133 HV. The relationship between hardness and grain size is described by the Hall-Petch law, with hardness being proportional to $1/\sqrt{d_{\mathrm{grain}}}$, where d is the mean grain size. This also indicates that each grain had no critical dislocations or low-angle grain boundaries. Fig. 7(c-1), (c-2), and (c-3) show the crystallinity of each grain. However, some band-shaped fine-grain areas were observed, which are the boundary areas between the laser-hatch trajectories. These grains were generated because the bead was rapidly cooled by the previous one. The mean grain size increased with an increase in the *VED* because the melt pool size increased with an increase in *VED*, the cooling speed decreased, the time during which the material was liquid increased, and increased crystal growth was promoted. The largest grain size was obtained at 400 W and 700 mm/s (c-3), and the standard deviation of the hardness was comparatively large. This indicates that the phenomena in the PBF-LB are unstable. The depth of the melt pool and aspect ratio for this sample were comparatively large, as shown in Fig. 5

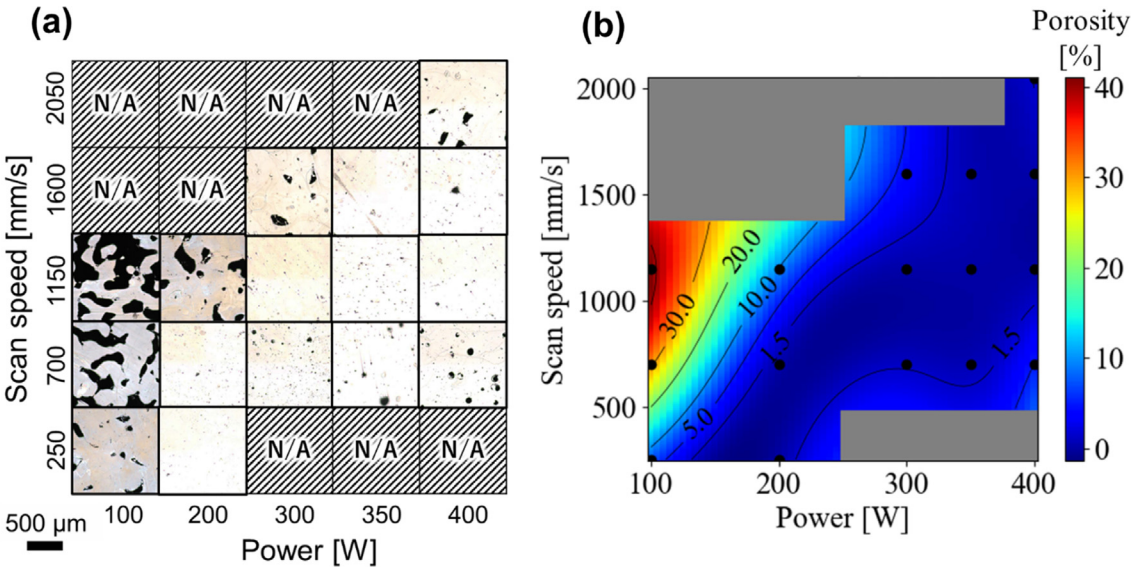

Fig. 6. (a) Cross-sectional optical images of bulk TPs, (b) map of porosity obtained by 3D-XCT.

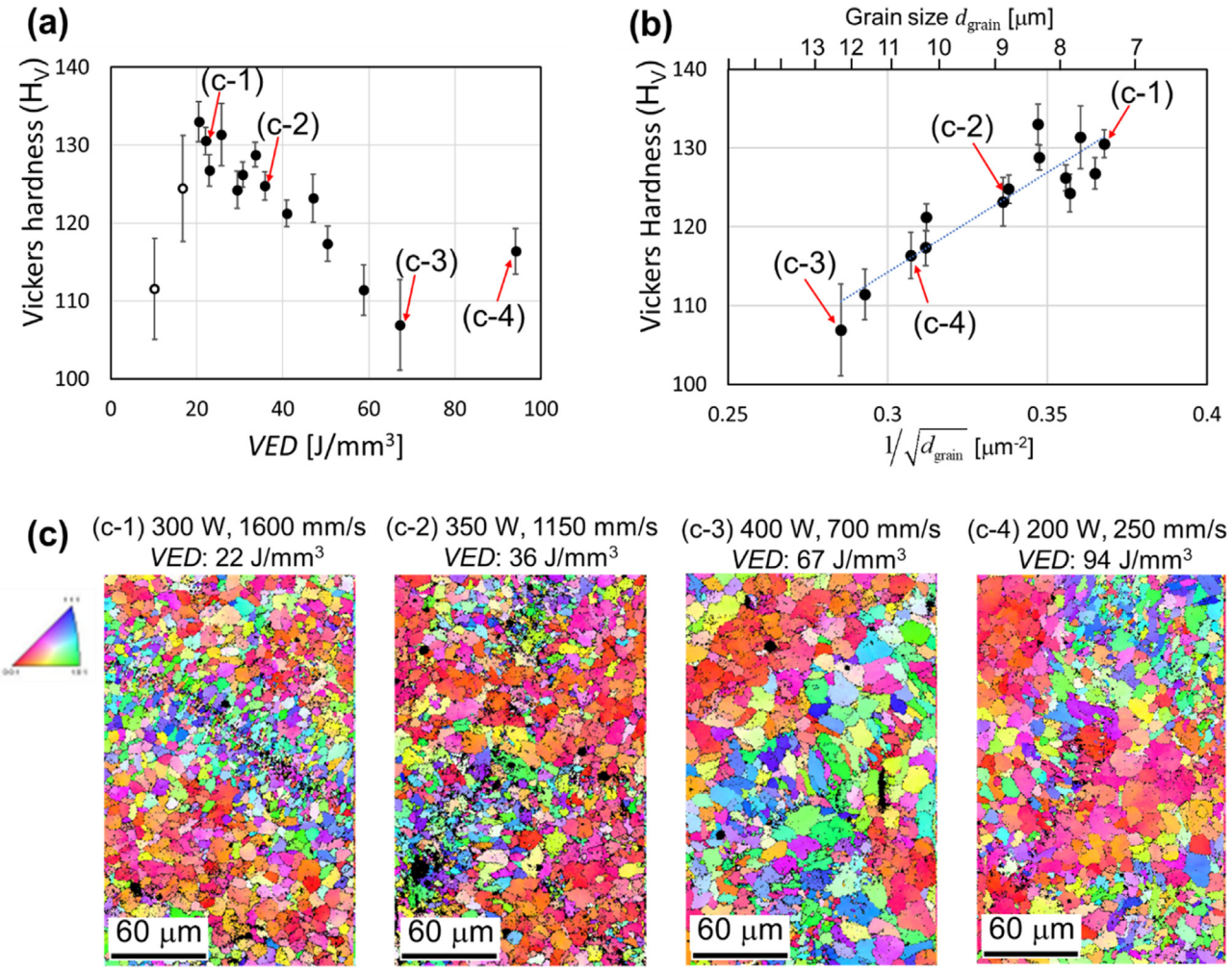

Fig. 7. Vickers hardness as functions of (a) *VED* (white circles indicate porosity greater than 10 %) and (b) grain size and (c) IPF maps of three parameter sets.

(a) and (b), respectively. As shown in Fig. 6(a), the porosity was comparatively large at 5 % owing to the gas pores.

Finally, a sample with a *VED* of 95 J/mm^3 is discussed. The sample was obtained at 200 W, 250 mm/s. The aspect ratio of a single bead and porosity of the bulk samples are both in the lowest areas, as shown in Fig. 5(b) and 6(b), respectively; however, the aspect ratio of a single bead in the neighboring parameter, 300 W, 250 mm/s, was larger, and the bulk TP was not successfully obtained. Therefore, this parameter is considered unstable.

High hardness can be achieved with a low risk of porosity formation at a *VED* of 20–50 J/mm^3.

5. Observation results and discussion

Fig. 8(a-1), (b-1), and (c-1) show three images with three parameter sets (*VED*s of 5.7, 22, and 190 J/mm^3) as the path of the laser progresses. In each figure, the powder and droplet spatter are marked, whose numbers are shown in Fig. 8(a-2), (b-2), and (c-2) at each point in time. The amount of spatter was characterized by the average number, and these values are discussed in the following section. The higher the *VED*, the larger is the amount of powder and droplet spatter. Fig. 8(a-3), (b-3), and (c-3) show schematics of the melt pool area, and a detailed discussion is presented in the next paragraph. Here, we notice a difference in the distribution of the spatter in Fig. 8(a-1), (b-1), and (c-1). With a higher *VED*, the amount of spatter in the counting area increased, and the spatter was distributed over a wider area, particularly in the upper region. One possible reason for this is that, when the scanning speed is low, the counting area moves slower, so that even if the spatter velocity is the same, the distribution area becomes wider. Regarding the case when the *VED* was 190 J/mm^3, some particles would fly ahead of the laser. This is because the argon gas flows from right to left, and sweeps away the spatter. In this study, we counted the total number of spatter particles in an area of 1.76 × 1.76 mm^2 behind the laser; however, to investigate the phenomena in more detail, parameters such as spatter velocity, flying angle, and distribution need to be studied using other image-treatment techniques.

Fig. 9 shows the captured images from the 25 parameter sets. Fig. 9(a) shows the original images, and Fig. 9(b) shows the same

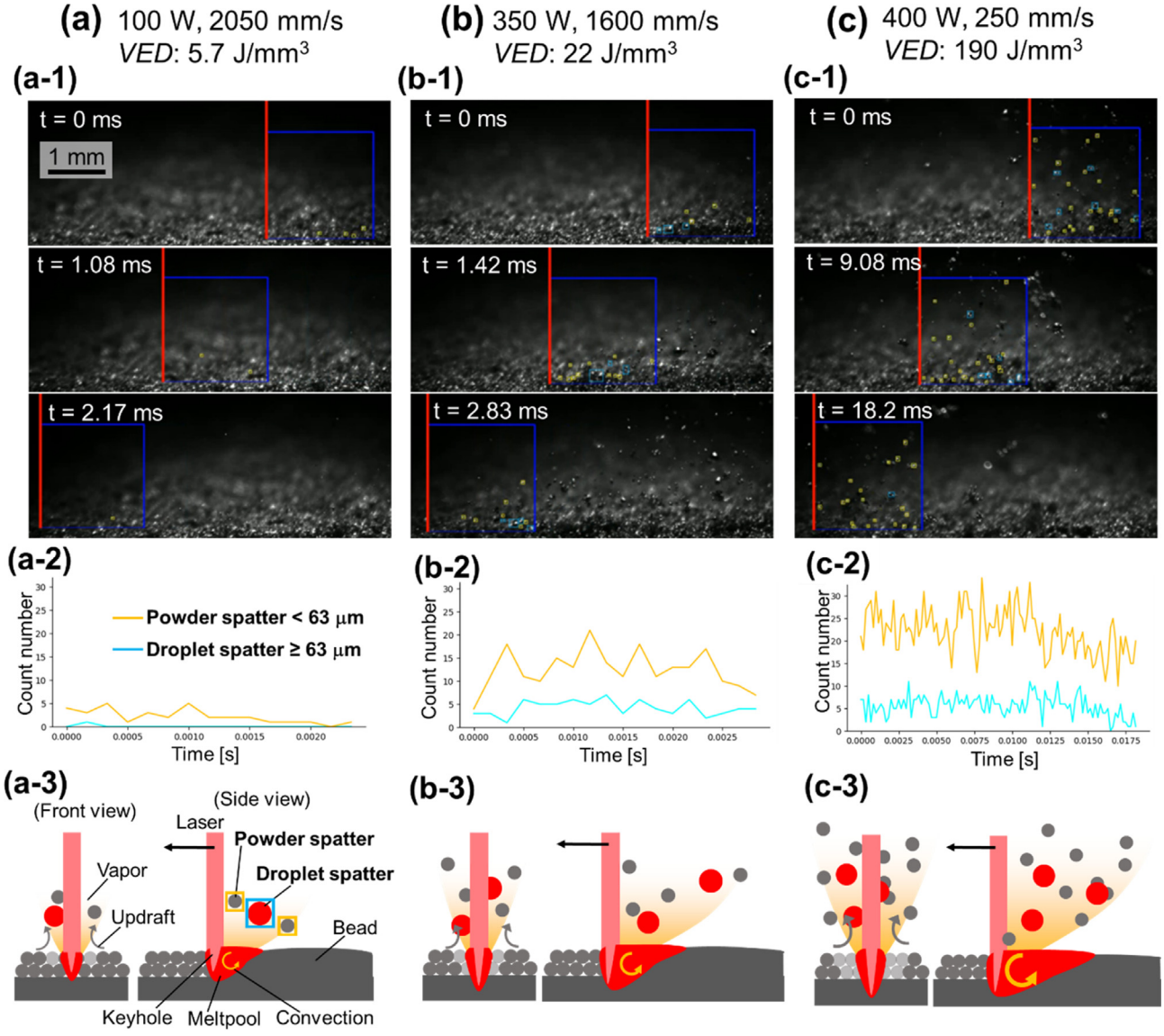

Fig. 8. (-1) Captured images, (-2) counted instances of spatter, (-3) schematics of melt pool and spatter, with three parameter sets, (a)100 W, 2050 mm/s, *VED*: 5.7 J/mm^3; (b) 350 W, 1600 mm/s, *VED*: 22 J/mm^3; (c) 400 W, 250 mm/s, *VED*: 190 J/mm^3.

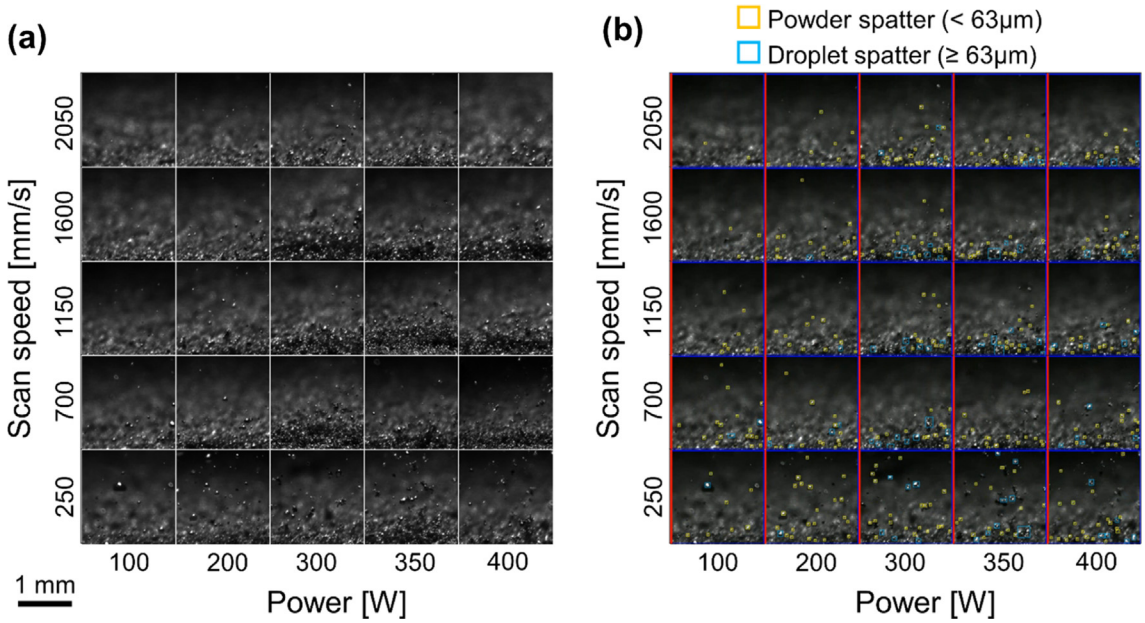

Fig. 9. Captured images with the area where spatters are counted (a) without and (b) with counting marks.

images with counting marks, laser (red line), area (blue box), powder spatter (yellow box), and droplet spatter (sky blue box). Fig. 10 shows the contour of number counts of (a) powder spatter and (b) droplet spatter. Overall, the amount of spatter is related to the *VED*, i.e., higher energy (bottom right) resulted in a greater amount of spatter. This can be explained using the schematics in Figs. (a-3), (b-3), and (c-3). First, the powder spatter amount is discussed. With a higher *VED*, an updraft owing to greater vapor pressure occurs, the non-melted powders in the bed around the irradiated area are agitated, and the amount of powder spatter increases [13]. To quantitatively investigate this updraft phenomenon, in-situ observation of plasma using a conventional high-speed observation system would be useful. Second, the amount of droplet spatter was analyzed. The droplet spatter is clearly related to the volume of the melt pool. A larger melt pool has more potential for droplet formation. A lower scanning speed gives the melt pool time to grow. Additionally, increased power causes increased recoil pressure resulting in a deeper keyhole and stronger convection in the melt pool. The recoil pressure produces the force needed to peel off droplets. The most dominant form of convection is Marangoni convection, which occurs owing to a gradient of surface tension in a melt pool with a high temperature gradient [32]. The intense convection destabilizes the melt pool surface. Therefore, a higher *VED*, i.e., lower scanning speed and higher power, results in a greater number of splatter particles.

A characteristic feature of the powder spatter in Fig. 10(a), that is, a feature that deviates from the tendency of the *VED*, is that there are two small hills in the middle-right and upper-middle portions with a basin in the center. The hills are considered to have occurred because the powder in the bed interacts with the droplet spatter created with increased power. Thus, a basin where the amount of spatter is a local minimum at the center occurs. We can compare this with Fig. 5(a) and the single bead that stably formed in the same central area. This can be rationalized by considering that a small amount of powder spatter means that the laser energy is efficiently used. By contrast, the droplet spatter has a hill in the middle-right area as shown in Fig. 10(b), similar to that observed in the powder spatter. When we compare the droplet spatter across the same power, the lower scanning speed produced a larger melt pool, while the temperature gradient in the scanning direction was lower, and surface stability improved. Thus, a trade-off relationship exists.

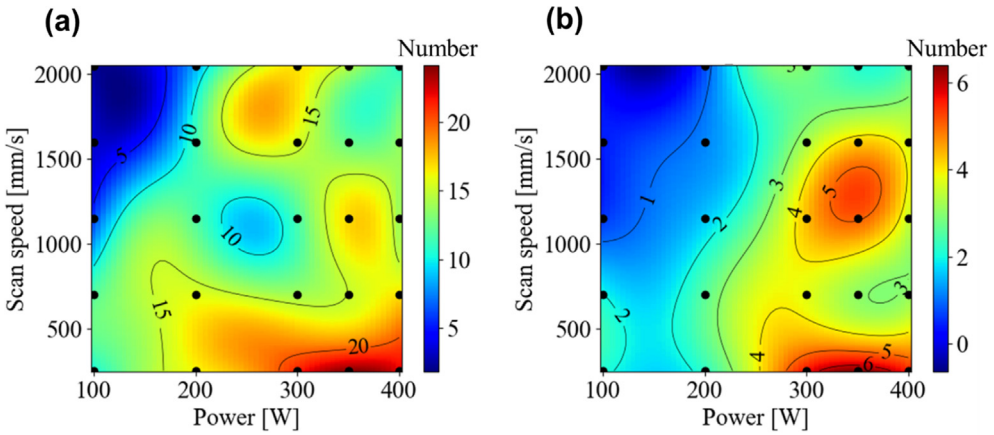

Fig. 10. Contour of (a) amount of powder spatter (<63 μm) and (b) amount of droplet spatter (≥63 μm).

In this study, the underlayer was fixed to the bulk layer printed using the standard recipe for observation; however, the heat conduction phenomenon changes depending on the parameters used for printing the underlayer, thereby causing the characteristics of the flying particles to be different. Moreover, these characteristics depend on whether it is the first bead or a subsequently printed bead with different hatch distances. For future work the parameters of underlayer and subsequent hatches should be considered as additional parameter spaces. However, from the viewpoint of this parameter exploration method, considering these parameters as fixed is useful.

6. Regression analysis of observed spatter

6.1. LASSO regression of porosity

As discussed in Section 4.2, porosity has a strong positive correlation with the reciprocal of the *VED*. We used the LASSO regression expressed in Eq. (6) to obtain the prediction models of Eqs. (2) and (4). The regularization coefficient λ was set to 0.001.

Table 4 lists the LASSO regression results for the coefficients. In the basic exponential model of Eq. (2), α_{po} was −0.44. In the case of the extended model of Eq. (4), in which the amounts of droplet and powder spatter were added as additional variables, there was a different exponent set. The exponent value for the amount of droplet spatter, γ_{po} (=-0.51), was greater than the amount of powder spatter, β_{po} (=0.09), although the counted number of powder spatter, n_{pow}, is usually larger than that of droplet spatter, n_{drop}. As shown in Fig. 11, in the case of the extended model of Eq. (4), the coefficient of determination, R^2, increased from 0.313 to 0.580, which demonstrates the feasibility of considering the amount of spatter in the prediction model. This improvement has also been discussed in previous studies [44,45]. To further improve the prediction accuracy, other feature values should be obtained from the captured images. This will be performed as part of our future work.

6.2. LASSO regression of Vickers hardness

As shown in Fig. 7(a), the Vickers hardness had a strong positive correlation with the reciprocal of the *VED*. However, they are not completely related to each other. Therefore, we added the amounts of droplet and powder spatter as variables, as shown in Eq. (5). Then, the LASSO regression of Eq. (6) was applied again to predict the Vickers hardness using the basic exponential model of Eq. (3) and extended model of Eq. (5).

Table 5 lists the LASSO regression results for the coefficients of the two models. In the basic model of Eq. (3), α_{vh} was −0.072 and the coefficient of determination R^2 (=0.29) was not sufficiently high, as shown in Fig. 12(a). However, in the case of Eq. (4), where the amounts of droplet and powder spatter were added as additional variables, the coefficients changed, as shown in Table 4, and R^2 improved to 0.55, which is still not sufficiently high; however, the prediction accuracy improved. It is also notable that the coefficients for the amount of spatter, β_{vh} and γ_{vh}, were positive, whereas α_{vh} for the *VED* was negative.

The predicted Vickers hardness values were plotted against the laser power and scanning speed and compared, as shown in Fig. 13. Fig. 13(a) shows the contour from the data obtained in the experiment, which is the same as that used in Fig. 7. There are two hills in the belt area from the bottom left to the upper right. Fig. 13(b) shows the predicted plots based on the basic model of Eq. (3), which has a monotonous gradient from the bottom right to the upper left. Finally, Fig. 13(c) shows the predicted plots based on the extended model of Eq. (5). In the figure, two hills are observed, the positions of which are not the same as in Fig. 13(a); however, the qualitative prediction accuracy was drastically improved compared to the prediction by Eq. (3), which only had the *VED* as a vari-

Table 4
LASSO regression results for prediction model of (2) and (4).

Coefficient / Constant	Value for (2)	Value for (4)
α_{po}	−0.44	−0.25
β_{po}	–	0.09
γ_{po}	–	−0.51
μ_{po}	1.38	1.38

Table 5
LASSO regression results for prediction model of (3) and (5).

Coefficient / Constant	Value for (3)	Value for (5)
α_{vh}	−0.07	−0.12
β_{vh}	–	0.04
γ_{vh}	–	0.06
μ_{vh}	18.62	18.62

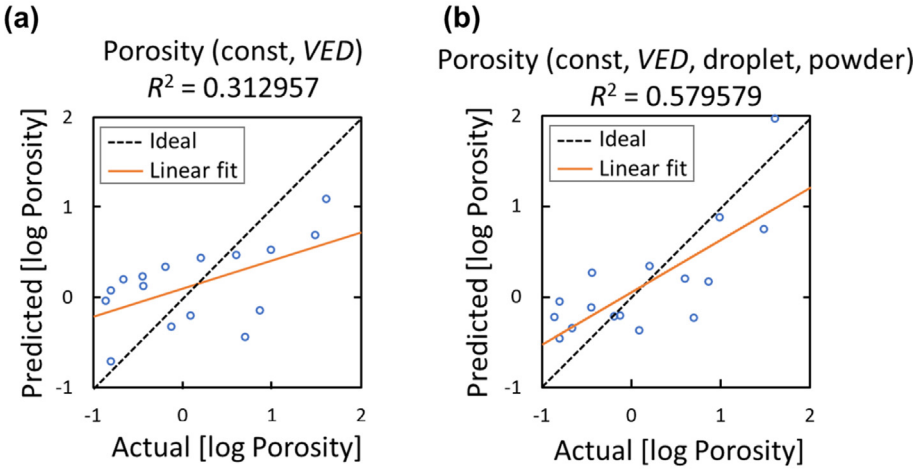

Fig. 11. Results of LASSO regression for the prediction model of porosity. (a) result of basic model of (2); (b) result of extended model of (4). Both show the actual-predicted plots in log scale, along with the coefficient of determination R^2.

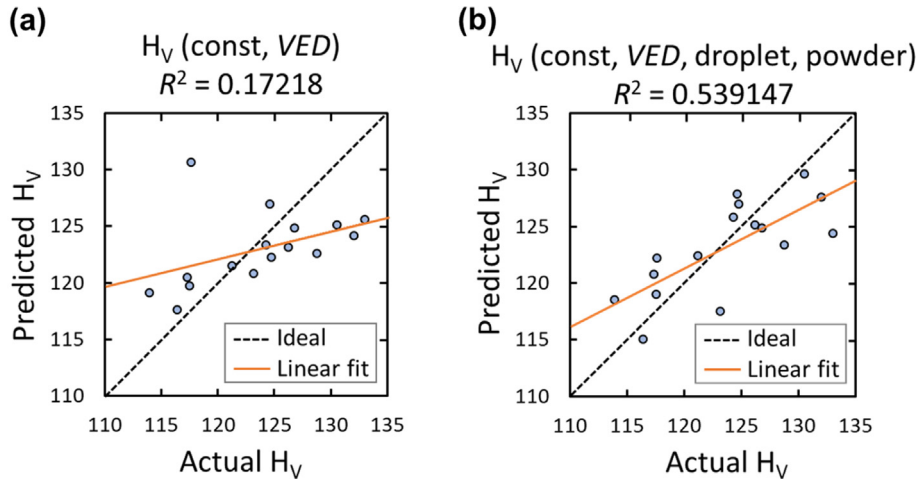

Fig. 12. Results of LASSO regression for the prediction model of Vickers hardness. (a) result of basic model of (3); (b) result of extended model of (5). Both shows the actual-predicted plots, along with the coefficient of determination R^2.

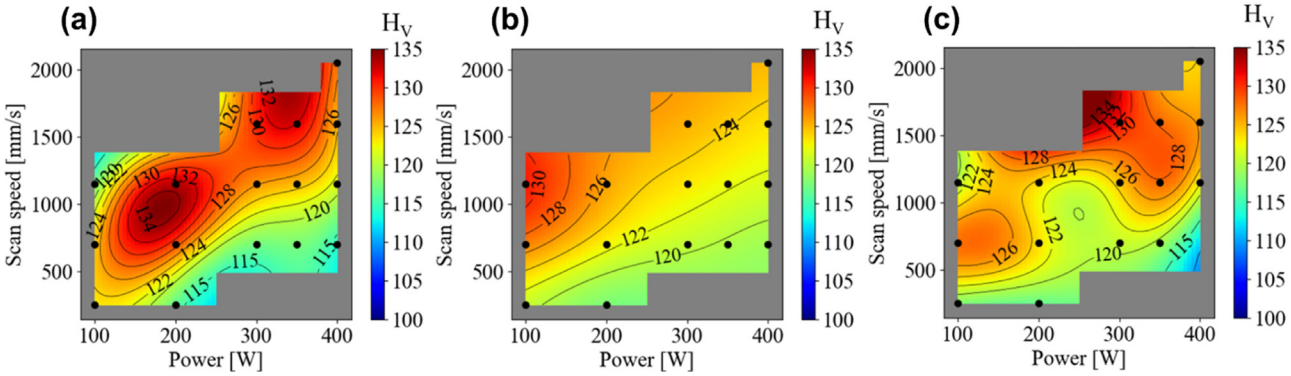

Fig. 13. Contours of (a) Vickers hardness experimentally obtained as functions of power and scanning speed, (b) predicted by basic model of (3), (c) predicted by extended model of (5).

able. In future, we should obtain more data and explore better feature values from the captured images based on the physical mechanism of PBF-LB, such as a finer differentiated size, shape, velocity, or flying angle of spatter particles. The feature values for the prediction of mechanical properties obtained in this study are expected to be strong objective functions for high-throughput parameter exploration represented by Bayesian optimization in powder manufacturing processes, which has complex physical phenomena and a huge parameter space [48–50].

7. Conclusion

This study proposed a prediction method for the mechanical properties of an aluminum alloy using dynamically observed flying particles at the synthesizing point of PBF-LB. A high-speed microscopic observation system was designed and built, and flying spatter particles were successfully observed. The observed spatter was differentiated as powder and droplet spatter based on the threshold diameter derived from the upper size limit of the original powder. The relationship between the amount of spatter counted by image treatment and the Vickers hardness of the bulk sample was investigated using LASSO regression analysis. By including the spatter numbers instead of using only the *VED*, the prediction quality represented by the coefficient of determination for the porosity and Vickers hardness were improved from 0.312 to 0.580 and from 0.172 to 0.539, respectively, thus showing the advantage of additional analysis of the powder during the process. For a higher prediction score, further candidates, such as a finer differentiated size, shape, velocity, or flying angle of spatter particles, should be investigated as the other feature values. This method will lead to a high-throughput process parameter exploration focused on optimizing mechanical properties such as hardness or porosity for various shapes, in which the optimal parameters are not necessarily the same because of the environment around the point of laser irradiation.

Data availability

No data was used for the research described in the article.

Declaration of Competing Interest

The authors declare that they have no known competing financial interests or personal relationships that could have appeared to influence the work reported in this paper.

Acknowledgement

We would like to thank Mr. Harald Frank, wbk, KIT, for his experimental setup and support of the observation experiment; Mr. George Kuwabara, Photron Ltd., for his support in the selection of observation optics; camera, objective lens, filter, and condition-

ing the parameters; Mr. Phillip Schwarz and Mr. Gregor Graf of Edelstahl Rosswag GmbH, for their advice on parameter changes for the single bead recipe in the SLM machine; Ms. Katja Höger, wbk, KIT, for her measurement of porosity in the bulk test pieces by 3D X-ray CT; Mr. Morio Tomizawa, Mr. Ryo Okawara and Mr. Justin Lach, from the University of Tokyo, for their support in image treatment and regression analysis. We would like to thank Dr. Yoshitaka Ushiku, Omron Scinic X Corporation, and Prof. Takayuki Osa, the University of Tokyo, for technical discussions on image treatment and regression analysis. This work was partially supported by JSPS Grant-in-Aid for Scientific Research(B), KAKENHI Grant Number JP22H01373.

Appendix A. Supplementary material

Supplementary data to this article can be found online at https://doi.org/10.1016/j.matdes.2023.111696.

References

[1] J. Gibson, D. Rosen, B. Stucker, Additive Manufacturing Technologies: Rapid Prototyping to Direct Digital Manufacturing, Springer, New York, 2009, pp. 123–130.
[2] V. Bhavar, P. Kattire, V. Patil, S. Khot, K. Gujar, R. Singh, Chapter, A Review on Powder Bed Fusion Technology of Metal Additive Manufacturing, Additive manufacturing handbook, CRC Press, 2017.
[3] W.E. King, A.T. Anderson, R.M. Ferencz, N.E. Hodge, C. Kamath, S.A. Khairallah, A.M. Rubenchik, Laser powder bed fusion additive manufacturing of metals; physics, computational, and materials challenges, Appl. Phys. Rev. 2 (2015), https://doi.org/10.1063/1.4937809 041304.
[4] S. Sanchez, P. Smith, Z. Xu, G. Gaspard, C.J. Hyde, W.W. Wits, I.A. Ashcroft, H. Chen, A.T. Clare, Powder Bed Fusion of nickel-based superalloys: A review, Int. J. Mach. Tools Manuf. 165 (2021) 103729.
[5] H. Gong, K. Rafi, H. Gu, T. Starr, B. Stucker, Analysis of defect generation in Ti–6Al–4V parts made using powder bed fusion additive manufacturing processes, Addit. Manuf. 1–4 (2014) 87–98, https://doi.org/10.1016/j.addma.2014.08.002.
[6] D.D. Gu, W. Meiners, K. Wissenbach, R. Poprawe, Laser additive manufacturing of metallic components: Materials, processes and mechanisms, Int. Mater. Rev. 57 (2012) 133–164, https://doi.org/10.1179/1743280411Y.0000000014.
[7] A.V. Gusarov, I. Yadroitsev, P. Bertrand, I. Smurov, Heat transfer modelling and stability analysis of selective laser melting, Appl. Surf. Sci. 254 (2007) 975–979, https://doi.org/10.1016/j.apsusc.2007.08.074.
[8] T. Qi, H. Zhu, H. Zhang, J. Yin, L. Ke, X. Zeng, Selective laser melting of Al7050 powder: Melting mode transition and comparison of the characteristics between the keyhole and conduction mode, Mater. Des. 135 (2017) 257–266, https://doi.org/10.1016/j.matdes.2017.09.014.
[9] S. Ly, A.M. Rubenchik, S.A. Khairallah, G. Guss, M.J. Matthews, Metal vapor micro-jet controls material redistribution in laser powder bed fusion additive manufacturing, Sci. Rep. 7 (2017) 4085, https://doi.org/10.1038/s41598-017-04237-z.
[10] H. Zheng, H. Li, L. Lang, S. Gong, Y. Ge, Effects of scan speed on vapor plume behavior and spatter generation in laser powder bed fusion additive manufacturing, J. Manuf. Processes. 36 (2018) 60–67, https://doi.org/10.1016/j.jmapro.2018.09.011.
[11] A.B. Anwar, Q.-C. Pham, Study of the spatter distribution on the powder bed during selective laser melting, Addit. Manuf. 22 (2018) 86–97, https://doi.org/10.1016/j.addma.2018.04.036.
[12] D. Wang, S. Wu, F. Fu, S. Mai, Y. Yang, Y. Liu, C. Song, Mechanisms and characteristics of spatter generation in SLM processing and its effect on the properties, Mater. Des. 117 (2017) 121–130, https://doi.org/10.1016/j.matdes.2016.12.060.
[13] M.J. Matthews, G. Guss, S.A. Khairallah, A.M. Rubenchik, P.J. Depond, W.E. King, Denudation of metal powder layers in laser powder bed fusion processes, Acta Mater. 114 (2016) 33–42, https://doi.org/10.1016/j.actamat.2016.05.017.
[14] N.T. Aboulkhair, I. Maskery, C. Tuck, I. Ashcroft, N.M. Everitt, On the formation of AlSi10Mg single tracks and layers in selective laser melting: Microstructure and nano-mechanical properties, J. Mater. Process. Technol. 230 (2016) 88–98, https://doi.org/10.1016/j.jmatprotec.2015.11.016.
[15] M. Simonelli, C. Tuck, N.T. Aboulkhair, I. Maskery, I. Ashcroft, R.D. Wildman, R. Hague, A study on the laser spatter and the oxidation reactions during selective laser melting of 316L stainless steel, Al-Si10-Mg, and Ti-6Al-4V, Metall. Mater. Trans. A. 46 (2015) 3842–3851, https://doi.org/10.1007/s11661-015-2882-8.
[16] I. Yadroitsev, P. Bertrand, G. Antonenkova, S. Grigoriev, I. Smurov, Use of track/layer morphology to develop functional parts by selective laser melting, J. Laser Appl. 25 (2013), https://doi.org/10.2351/1.4811838 052003.
[17] V. Gunenthiram, P. Peyre, M. Schneider, M. Dal, F. Coste, I. Koutiri, R. Fabbro, Experimental analysis of spatter generation and melt-pool behavior during the powder bed laser beam melting process, J. Mater. Process. Technol. 251 (2018) 376–386, https://doi.org/10.1016/j.jmatprotec.2017.08.012.
[18] D. Ye, K. Zhu, J.Y.H. Fuh, Y. Zhang, H.G. Soon, The investigation of plume and spatter signatures on melted states in selective laser melting, Opt. Laser Technol. 111 (2019) 395–406, https://doi.org/10.1016/j.optlastec.2018.10.019.
[19] U. Ali, R. Esmaeilizadeh, F. Ahmed, D. Sarker, W. Muhammad, A. Keshavarzkermani, Y. Mahmoodkhani, E. Marzbanrad, E. Toyserkani, Identification and characterization of spatter particles and their effect on surface roughness, density and mechanical response of 17–4 PH stainless steel laser powder-bed fusion parts, Mater. Sci. Eng. A. 756 (2019) 98–107, https://doi.org/10.1016/j.msea.2019.04.026.
[20] A.A. Martin et al., Dynamics of pore formation during laser powder bed fusion additive manufacturing, Nat. Commun. 10 (2019) 1987, https://doi.org/10.1038/s41467-019-10009-2.
[21] N.T. Aboulkhair, N.M. Everitt, I. Ashcroft, C. Tuck, Reducing porosity in AlSi10Mg parts processed by selective laser melting, Addit. Manuf. 1–4 (2014) 77–86, https://doi.org/10.1016/j.addma.2014.08.001.
[22] T. Guraya, S. Singamneni, Z.W. Chen, Microstructure formed during selective laser melting of IN738LC in keyhole mode, J. Alloys Compd. 792 (2019) 151–160, https://doi.org/10.1016/j.jallcom.2019.03.419.
[23] X. Liu, C. Zhao, X. Zhou, Z. Shen, W. Liu, Microstructure of selective laser melted AlSi10Mg alloy, Mater. Des. 168 (2019), https://doi.org/10.1016/j.matdes.2019.107677 107677.
[24] H. Qin, V. Fallah, Q. Dong, M. Brochu, M.R. Daymond, M. Gallerneault, Solidification pattern, microstructure and texture development in Laser Powder Bed Fusion (LPBF) of Al10SiMg alloy, Mater. Char. 145 (2018) 29–38, https://doi.org/10.1016/j.matchar.2018.08.025.
[25] A.B. Anwar, Q.-C. Pham, Selective laser melting of AlSi10Mg: Effects of scan direction, part placement and inert gas flow velocity on tensile strength, J. Mater. Process. Technol. 240 (2017) 388–396, https://doi.org/10.1016/j.jmatprotec.2016.10.015.
[26] M. Skalon, B. Meier, A. Gruberbauer, S.T. Amancio-Filho, C. Sommitsch, Stability of a Melt Pool During 3D-Printing of an Unsupported Steel Component and Its Influence on Roughness, Materials 13 (2020) 808.
[27] S.A. Khairallah, A. Anderson, Mesoscopic simulation model of selective laser melting of stainless steel powder, J. Mater. Process. Technol. 214 (2014) 2627–2636, https://doi.org/10.1016/j.jmatprotec.2014.06.001.
[28] Y. Li, D. Gu, Thermal behavior during selective laser melting of commercially pure titanium powder: Numerical simulation and experimental study, Addit. Manuf. 1–4 (2014) 99–109, https://doi.org/10.1016/j.addma.2014.09.001.
[29] B. Liu, G. Fang, L. Lei, W. Liu, A new ray tracing heat source model for mesoscale CFD simulation of selective laser melting (SLM), Appl. Math. Modell. 79 (2020) 506–520, https://doi.org/10.1016/j.apm.2019.10.049.
[30] E. Soylemez, High deposition rate approach of selective laser melting through defocused single bead experiments and thermal finite element analysis for Ti-6Al-4V, Addit. Manuf. 31 (2020), https://doi.org/10.1016/j.addma.2019.100984 100984.
[31] D. Dai, D. Gu, Influence of thermodynamics within molten pool on migration and distribution state of reinforcement during selective laser melting of AlN/AlSi10Mg composites, Int. J. Mach. Tool. Manuf. 100 (2016) 14–24, https://doi.org/10.1016/j.ijmachtools.2015.10.004.
[32] T.-N. Le, Y.-L. Lo, Effects of sulfur concentration and Marangoni convection on melt-pool formation in transition mode of selective laser melting process, Mater. Des. 179 (2019), https://doi.org/10.1016/j.matdes.2019.107866 107866.
[33] M. Grasso, B.M. Colosimo, Process defects and in situ monitoring methods in metal powder bed fusion: A review, Meas. Sci. Technol. 28 (2017), https://doi.org/10.1088/1361-6501/aa5c4f 044005.
[34] C. Zhao, K. Fezzaa, R.W. Cunningham, H. Wen, F.D. De Carlo, L. Chen, A.D. Rollett, T. Sun, Real-time monitoring of laser powder bed fusion process using high-speed X-ray imaging and diffraction, Sci. Rep. 7 (2017) 3602, https://doi.org/10.1038/s41598-017-03761-2.
[35] Q. Guo, C. Zhao, M. Qu, L. Xiong, L.I. Escano, S.M.H. Hojjatzadeh, N.D. Parab, K. Fezzaa, W. Everhart, T. Sun, L. Chen, In-situ characterization and quantification of melt pool variation under constant input energy density in laser powder bed fusion additive manufacturing process, Addit. Manuf. 28 (2019) 600–609, https://doi.org/10.1016/j.addma.2019.04.021.
[36] L. Mazzoleni, A.G. Demir, L. Caprio, M. Pacher, B. Previtali, Real-time observation of melt pool in selective laser melting: Spatial, temporal, and wavelength resolution criteria, IEEE Trans. Instrum. Meas. 69 (2019) 1179–1190, https://doi.org/10.1109/TIM.2019.2912236.
[37] W.E. King, H.D. Barth, V.M. Castillo, G.F. Gallegos, J.W. Gibbs, D.E. Hahn, C. Kamath, A.M. Rubenchik, Observation of keyhole-mode laser melting in laser powder-bed fusion additive manufacturing, J. Mater. Process. Technol. 214 (2014) 2915–2925, https://doi.org/10.1016/j.jmatprotec.2014.06.005.
[38] H. Krauss, T. Zeugner, M.F. Zaeh, Layerwise monitoring of the selective laser melting process by thermography, Phys. Procedia. 56 (2014) 64–71, https://doi.org/10.1016/j.phpro.2014.08.097.
[39] S.K. Everton, M. Hirsch, P. Stravroulakis, R.K. Leach, A.T. Clare, Review of in-situ process monitoring and in-situ metrology for metal additive manufacturing, Mater. Des. 95 (2016) 431–445, https://doi.org/10.1016/j.matdes.2016.01.099.
[40] M.T. Andani, R. Dehghani, M.R.K. Ravari, R. Mizaeifar, J. Ni, A study on the effect of energy input on spatter particles creation during selective laser melting process, Addit. Manuf. 20 (2018) 33.

[41] S. Suzuki, K. Abe, Topological structural analysis of digitized binary images by border following, Comput. Graph. Image Process. 30 (1985) 32–46, https://doi.org/10.1016/0734-189X(85)90016-7.
[42] N. Singla, Motion detection based on frame difference method, Int. J. Inf. Comput. Technol. 4 (2014) 15.
[43] A. Kaehler, G. Bradski, Learning OpenCV 3, O'Reilly Media, Inc., 2016.
[44] F.E. Harrell Jr., Regression Modeling Strategies: With Applications to Linear Models, Logistic Regression, and Survival Analysis, 608, Springer, New York, 2001.
[45] A.E. Hoerl, R.W. Kennard, Ridge regression: Biased estimation for nonorthogonal problems, Technometrics. 12 (1970) 1–15.
[46] R. Tibshirani, Regression shrinkage and selection via the lasso, J. R. Stat. Soc. B. 58 (1996) 267–288, https://doi.org/10.1111/j.2517-6161.1996.tb02080.x.
[47] A.A. Martin, N.P. Calta, S.A. Khairallah, J. Wang, P.J. Depond, A.Y. Fong, V. Thampy, G.M. Guss, A.M. Kiss, K.H. Stone, C.J. Tassone, J.N. Weker, M.F. Toney, T. Burren, M.J. Matthews, Dynamics of pore formation during laser powder bed fusion additive manufacturing, Nat. Commun. 10 (2019) 1987, https://doi.org/10.1038/s41467-019-10009-2.
[48] Y. Tu, Z. Liu, L. Carneiro, C.M. Ryan, A.C. Parnell, S.B. Leen, N.M. Harrison, Towards an instant structure-property prediction quality control tool for additive manufactured steel using a crystal plasticity trained deep learning surrogate, Mater. Des. 213 (2022), https://doi.org/10.1016/j.matdes.2021.110345 110345.
[49] R. Taura, T. Osada, K. Minagawa, T. Kohata, M. Hirosawa, K. Tsuda, K. Kawaguchi, Machine learning-driven optimization in powder manufacturing of Ni-Co based superalloy, Mater. Des. 198 (2021), https://doi.org/10.1016/j.matdes.2020.109290 109290.
[50] K. Nagai, T. Osa, G. Inoue, T. Tsujiguchi, T. Araki, Y. Kuroda, M. Tomizawa, K. Nagato, Sample-efficient parameter exploration of the powder film drying process using experiment-based Bayesian optimization, Sci. Rep. 12 (2022) 1615, https://doi.org/10.1038/s41598-022-05784-w.